Journal of the European Ceramic Society 22 (2002) 263–270
www.elsevier.com/locate/jeurceramsoc

Superplastic behavior of liquid-phase sintered β-SiC prepared with oxynitride glasses in an N_2 atmosphere

Takayuki Nagano[a,*], Kenji Kaneko[a], Guo-Dong Zhan[b], Mamoru Mitomo[b], Young-Wook Kim[c]

[a]*Ceramics Superplasticity Project, ICORP, Japan Science and Technology Corporation, 2-4-1, Mutsuno, Atsuta-ku, Nagoya 456-8587, Japan*
[b]*National Institute for Research in Inorganic Materials, 1-1, Namiki, Tsukuba 305-0044, Japan*
[c]*The University of Seoul, 90 Cheonnong-dong, Tongdaemun-gu, Seoul 130-743, South Korea*

Received 16 November 2000; received in revised form 28 February 2001; accepted 7 March 2001

Abstract

The superplastic behavior of liquid-phase sintered β-SiC with oxynitride glasses was compared in compression and tension tests at 1973–2048 K in an N_2 atmosphere. Strain hardening was observed under all experimental conditions. Stress exponents in the compression tests of SiC with different additives were about 2 in the temperature ranging from 1973 to 2023 K. Amorphous phases were observed at the grain boundaries and at multi-grain junctions in the as-sintered materials. Superplastic behavior was greatly influenced by grain growth, vaporization of grain-boundary phase and formation of crystalline phase during tensile deformation.

Keywords: Creep; Grain boundaries; Mechanical properties; Plasticity; SiC

1. Introduction

SiC is a difficult material to densify without additives because of the covalent nature of Si–C bonding and its low self-diffusion coefficient. Boron and carbon have been most popular sintering additives for SiC[1] because boron (<0.3%) does not form an amorphous phase at the grain boundaries[2] and superior mechanical strength at elevated temperatures can be expected.

Superplasticity of SiC (140%) was discovered in B, C-doped β-SiC with a grain size of 0.2 μm fabricated by ultrahigh-pressure hot-isostatic-pressing (UHP–HIP) using a glass capsule in 1998.[3] In this material, boron segregation was found at two-grain junctions.[4] Therefore, the presence of boron at grain boundaries was thought to promote grain-boundary sliding which is the main mechanism of superplasticity.

On the other hand, liquid-phase sintered SiC with an amorphous phase at grain boundaries was thought to be easily deformed in comparison with solid-phase sintered SiC with no amorphous phase at grain boundaries. The authors of this study investigated the high temperature deformation of liquid-phase sintered β-SiC with the additions of oxide additives. However, they did not show superplastic deformation (>100%) due to the rapid grain growth, the vaporization of the grain-boundary phase and the decomposition of SiC.[5–8]

The authors of this study also investigated the effect of atmosphere on the weight loss of liquid-phase sintered β-SiC with oxide additives during the heat treatment, and found that the weight loss in N_2 was suppressed about 1/2 to 1/3 in comparison with the weight loss in Ar.[9] Although we performed the tension test of liquid-phase sintered β-SiC with oxide additives in N_2, the maximum tensile elongation reached only about 11% because of the crystallization of the grain-boundary phase.[10,11]

It was reported that the microstructure of SiC with the addition of oxynitride glass was stable at elevated temperatures in N_2, and grain growth and phase transformation in N_2 was suppressed in comparison with that in Ar.[12,13] Accordingly, the deformation of liquid-phase sintered SiC with oxynitride glass in N_2 has the merits of suppression of the grain growth, the phase transformation from β to α, the vaporization of liquid phase and the decomposition of SiC. Moreover, the

---

* Corresponding author.
E-mail address: t_nagano@jfcc.or.jp (T. Nagano).

PII: S0955-2219(01)00258-8

viscosity of the liquid phase with nitrogen is higher than that without nitrogen,[14] and the occurrence of cavitation should be suppressed.

Therefore, we fabricated liquid-phase sintered β-SiC with different oxynitride glasses and then compared the deformation behavior at elevated temperature in N_2 and microstructural change before and after the deformation.

2. Experimental procedure

2.1. Specimen preparation

The starting material was ultra fine β-SiC powder (T-1 grade, Sumitomo-Osaka Cement Co., Tokyo, Japan) fabricated by the chemical vapor deposition (CVD) method. It was oxidized at 873 K for 1 h in air, to eliminate free carbon, and treated with hydrofluoric acid, to remove SiO_2. The particle size was ~90 nm as calculated from the specific surface area. The mixtures of SiO_2 (reagent grade, Kanto Chemical Co., Tokyo, Japan), MgO (high purity grade, Wako Pure Chemical Industries, Ltd., Osaka, Japan), Al_2O_3 (99.9% pure, Sumitomo Chemical Co., Tokyo, Japan), Y_2O_3 (99.9% pure, Shin-Etsu Chemical Co., Tokyo, Japan), and AlN (F Grade, Tokuyama Soda Co., Tokyo, Japan) were prepared to oxynitride compositions by SiC ball milling in *n*-hexane as shown in Table 1. SiC was then mixed with 9 wt.% oxynitride powders by SiC ball milling in *n*-hexane. The mixed powder was hot-pressed at 2073 K under a stress of 30 MPa in N_2.

The as-sintered body was cut by diamond cutter and ground by diamond wheel. The size of compressive specimen was 2×2×3 mm. The specimen surfaces were mirror-polished with diamond pastes. The tensile specimen was dog-bone shape, having rectangular cross section (1×0.8 mm) with the gauge length of 4.4 mm. The gauge portion of the tensile specimen was also mirror-polished with diamond paste of 6 μm.

2.2. Compression and tension test

Compression test and tension test at constant cross-head speeds were performed by using a universal testing machine with a furnace at the initial strain rates from 1×10^{-4} s^{-1} to 5×10^{-6} s^{-1} at the temperature ranging from 1973 to 2048 K in N_2. The degree of specimen deformation was evaluated from the displacement of the crosshead. Compressive and tensile directions were perpendicular to the hot-pressing direction.

True strain (ε_t) is defined as

$$\varepsilon_t = \ln(l/l_0) \tag{1}$$

where l and l_0 are the deformed and original gauge length, respectively.

By assuming a homogeneous deformation process, the true stress (σ_t) can be calculated by the following relation:

$$\sigma_t = P/A_0 \ \exp(\varepsilon_t) \tag{2}$$

where P is the applied load and A_0 is the cross-section of the original specimen.

The strain rate ($\dot{\varepsilon}$) at elevated temperature can be expressed as[15]

$$\dot{\varepsilon} = A \ \sigma^n/\mathrm{d}^P \ \exp(-Q/RT) \tag{3}$$

where A is a constant, σ is the stress, d is the grain size, Q is the apparent activation energy, R is the gas constant, n is the stress exponent, and P is the exponent of the inverse grain size.

2.3. Microstructural observation

Both specimens SiC(G1) and SiC(G2) were observed before and after the deformation experiment using scanning electron microscopy (SEM: JSM-6330F, Jeol, Tokyo, Japan) on the polished and the plasma-etched surface with CF_4+O_2 (8%) gas. The average grain size is defined by the linear intercept length, as follows:

$$d_{av} = 1.776L \tag{4}$$

Here, d_{av} is the average grain size and L is the linear intercept length. X-ray analysis was also conducted (Model No. RINT2500, Rigaku, Tokyo, Japan). The polytypes of SiC were calculated using the method of Tanaka and Iyi.[16] Each specimen was cut perpendicular to the compressive axis and prepared by polishing and argon-ion-beam thinning for transmission electron microscopy (TEM) observation. High-resolution

Table 1
Chemical compositions and some properties of as-sintered materials

Material	Additives (wt.%)					Grain size (nm)	Density (g/cm^3)	Sintering condition
	SiO_2	MgO	Al_2O_3	Y_2O_3	AlN			
SiC(G1)	3.78	0.981	1.17	2.13	0.936	260	3.15	2073 K 30 MPa 20 min in N_2
SiC(G2)			5.022	3.321	0.657	230	3.21	2073 K 30 MPa 15 min in N_2

transmission electron microscopy (HRTEM) observation and energy dispersive X-ray spectroscopy (EDX) analysis were performed by 200 kV TEM (JEM-2010MD, Jeol, Tokyo, Japan) at a point-to-point resolution of 0.18 nm. Electron energy loss spectroscopy (EELS) analysis was performed by a scanning transmission electron microscope (Model No. HB601UX, VG Microscopes, East Grinstead, UK) with a minimum probe size of 0.22 nm.

3. Results

3.1. Mechanical behavior

3.1.1. Compression test

The true stress–true strain curves at 1998 K are shown in Fig. 1. No cracks were observed in both compressed specimens. SiC(G1) showed higher flow stress and higher strain hardening in comparison with SiC(G2).

The relationship between flow stress and strain rate is shown in Fig. 2. Flow stress was determined by the value at the true strain of −0.1. Flow stress of SiC(G1) was higher than that of SiC(G2). Flow stress of SiC(G1) at 2048 K was slightly lower than that of SiC(G1) at 2023 K. Stress exponents calculated from the slope of lines were about 2 in both SiC(G1) and SiC(G2).

3.1.2. Tension test

The true stress–true strain curves at 2023 K are shown in Fig. 3. Strain hardening was observed in both SiC(G1) and SiC(G2). SiC(G1) showed higher strain hardening and fractured at 74% elongation. On the other hand, SiC(G2) showed strain hardening till 110% elongation and then showed strain softening. The elongation of SiC(G2) finally achieved 153% elongation. Maximum true stresses were about 70 MPa in both SiC(G1) and SiC(G2).

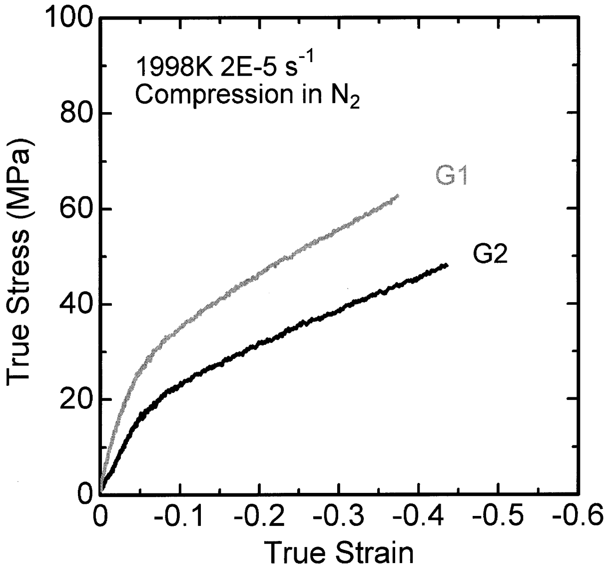

Fig. 1. True stress–true strain curves at 1998 K in compression tests.

3.2. Microstructural change

3.2.1. As-sintered materials

SEM photographs of as-sintered materials are shown in Fig. 4. The average grain sizes of SiC(G1) and SiC(G2) were 260 and 230 nm, respectively. The orientation of grains was not observed in both SiC(G1) and SiC(G2). Most of the grains were equiaxed shape and grain-boundary phases were observed in both SiC(G1) and SiC(G2). The grains of SiC(G2) were fully wetted.

HRTEM images at grain boundaries are shown in Fig. 5. An amorphous phase from 1 to 2 nm was evident in SiC(G1) and SiC(G2). However, some grain

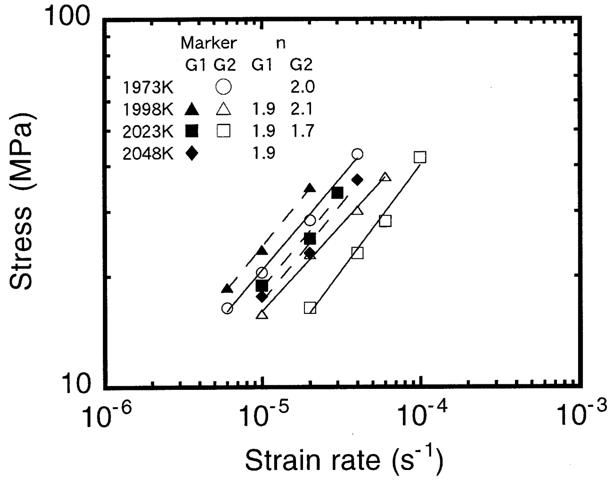

Fig. 2. Relationship between flow stress and strain rate.

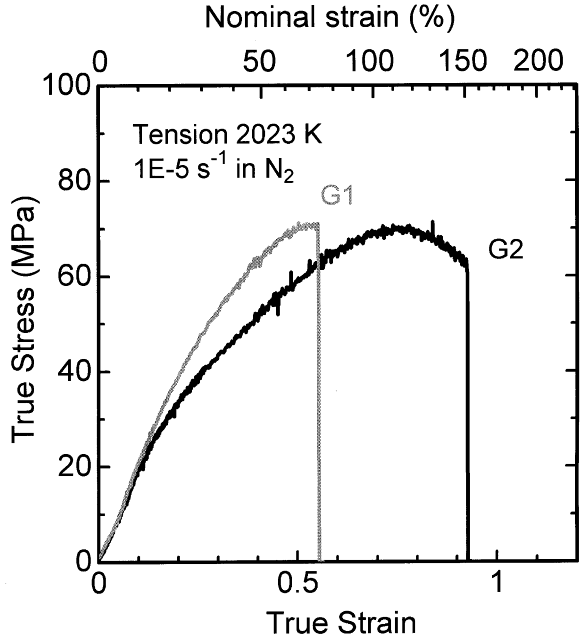

Fig. 3. True stress–true strain curves at 2023 K in tension tests.

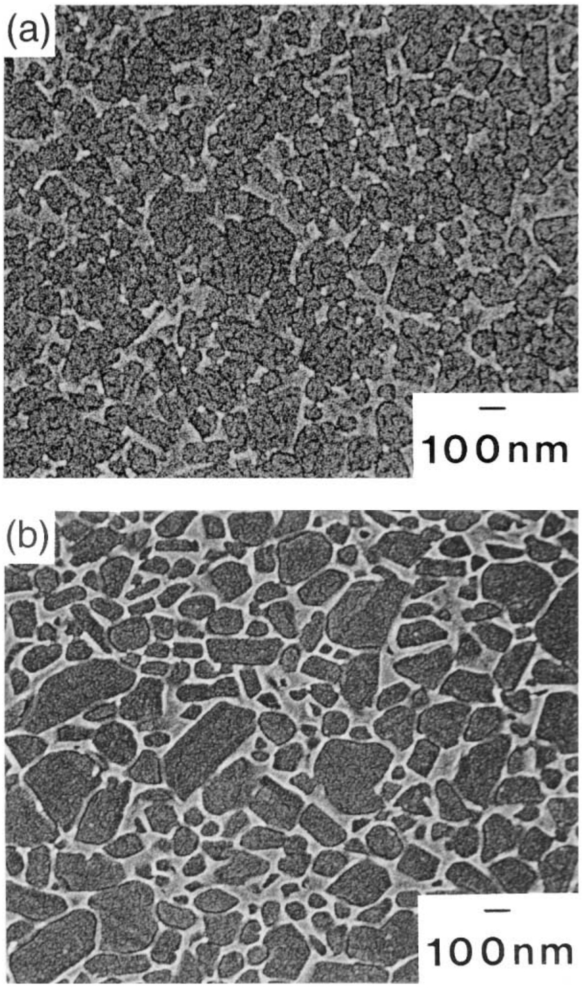

Fig. 4. SEM photographs of as-sintered materials of (a) SiC(G1) and (b) SiC(G2).

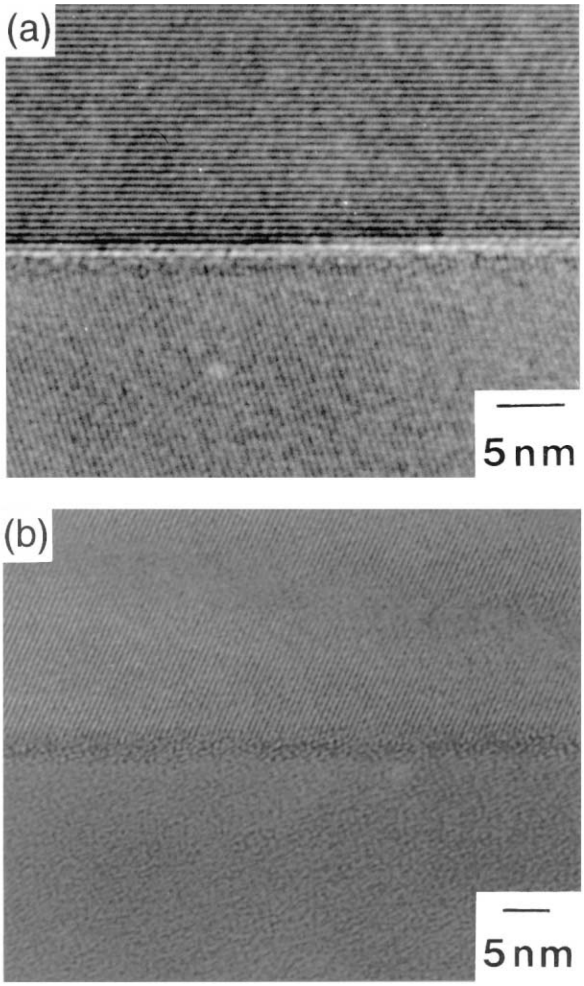

Fig. 5. HRTEM images at grain boundaries of (a) SiC(G1) and (b) SiC(G2) in as-sintered materials.

boundaries with no amorphous phase were observed in SiC(G1).

Energy-loss near-edge structure (ELNES) results for as-sintered materials are shown in Figs. 6 and 7. The peaks for Mg–L, Al–L, Si–L and O–K were detected at the grain boundary of SiC(G1). Moreover, Y–M peak was observed at the grain boundary region of SiC(G1) in EDX result. On the other hand, the peaks for Al–L, Si–L, O–K and N–K were detected at the grain boundary of SiC(G2). Moreover, Y–M peak was observed at the grain boundary of SiC(G2) in EDX result.

3.2.2. *Dynamic change*

SEM photographs of compressed materials are shown in Fig. 8. The distribution of the grain-boundary phase in compressed SiC(G1) became more inhomogeneous and many grains that are apparently directly bonded were observed. On the other hand, grains of compressed SiC(G2) were elongated in the perpendicular direction of the compressive axis. The grain aspect ratio was ~0.82 in the direction of compressive axis.

SEM photographs at gauge portions of elongated specimens are shown in Fig. 9. The cavitation damage of SiC(G1) after 74% elongation was higher than that of SiC(G2) after 153% elongation. The average grain sizes of SiC(G1) after 74% elongation were 350 and 500 nm in the vertical and horizontal directions of tensile axis, respectively. On the other hand, the average grain sizes of SiC(G2) after 153% elongation were 300 and 430 nm in the vertical and horizontal directions of tensile axis, respectively. Most of the residual grain-boundary phase after 153% elongation existed at the triple points.

Intergranular strain (ε_g) is defined as follows:[17]

$$\varepsilon_g = \ln\left(d_{//}/d_{\perp}^{2}\cdot d_{//}\right)^{1/3} = 2/3\ln\left(d_{//}/d_{\perp}\right) \quad (5)$$

where $d_{//}$ is the grain size parallel to the tensile axis and $d_{\perp}$ is the grain size perpendicular to the tensile axis. The ratio of intergranular strain to the total strain ($\varepsilon_{\mathrm{total}}$) is calculated to be about 24%. If we assume that the total strain is the sum of intergranular strain and the strain by grain-boundary sliding, the strain caused by

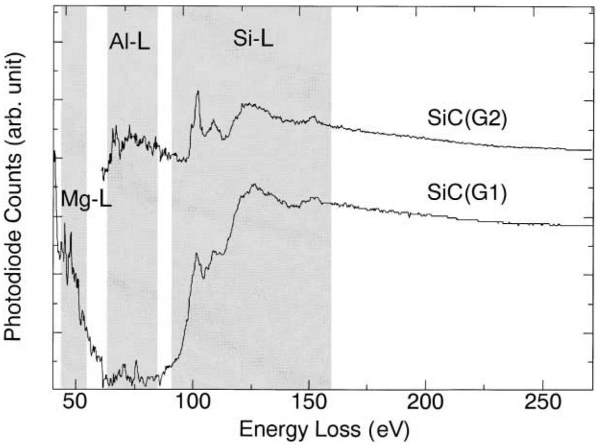

Fig. 6. ELNES at Mg–L edges, Al–L edges, and Si–L edges for as-sintered materials.

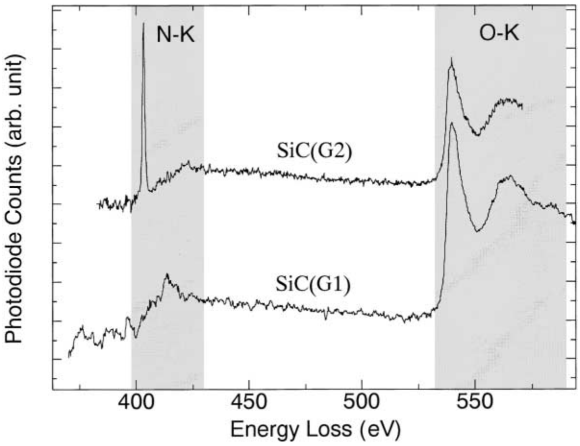

Fig. 7. ELNES at N–K edge, and O–K edge for as-sintered materials.

grain-boundary sliding is roughly estimated to be in the order of 76% in both SiC(G1) and SiC(G2).[18]

HRTEM images of the gauge portion after the tensile deformation are shown in Fig. 10. The amorphous phase mostly disappeared at many grain boundaries in SiC(G1). A crystalline phase was observed at the triple points of SiC(G1). The EDX result showed that the crystalline phase at the triple points contained *Y*. The concentration of other elements was below the detection limit. On the other hand, the amorphous phase was remaining at many grain boundaries of SiC(G2). A crystalline phase was also observed at the triple points of SiC(G2). The EDX result showed that the crystalline phase at triple points contained Y, Al and O.

3.3. XRD analysis

Crystalline phase of as-sintered materials was almost β-SiC(3C) single phase. In compressed specimens of SiC(G1) and SiC(G2), the phase transformation from β to α was less than 1%.

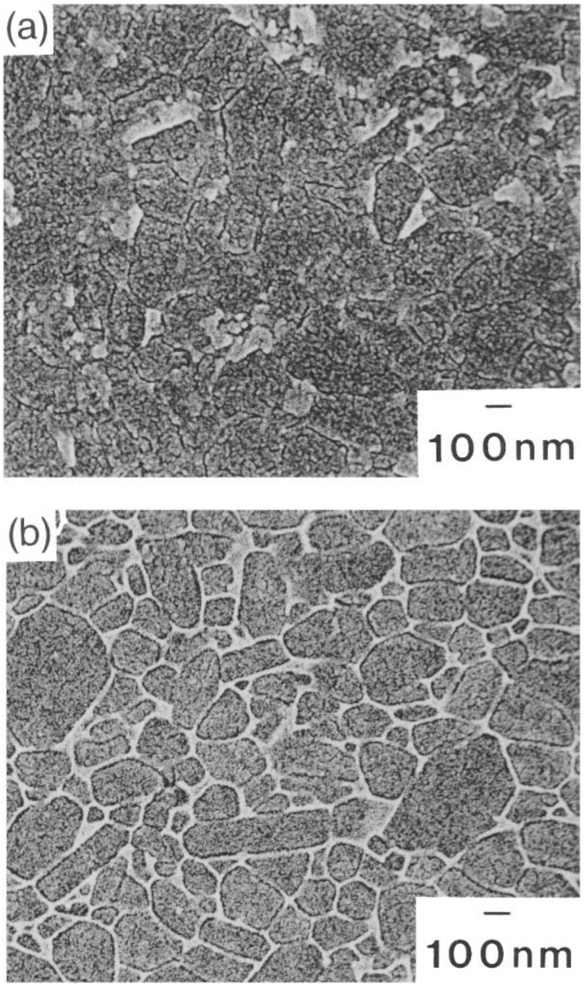

Fig. 8. SEM photographs of compressed (a) SiC(G1) and (b) SiC(G2) (1998 K, 4×10^{-5} s^{-1}, 35% strain, compression axis is vertical).

On the other hand, in the case of elongated specimens of SiC(G1) and SiC(G2), the phase of α-SiC(6H) was observed. The contents of α-SiC for the elongated specimens of SiC(G1) and SiC(G2) were calculated to be about 20%.

The crystalline phases, which were formed after tensile deformations of SiC(G1) and SiC(G2), were not detected by XRD analysis.

4. Discussion

4.1. Comparison between compressive deformation and tensile deformation

Some materials indicate the different deformation behavior in compression and tension tests at same experimental conditions. Luecke et al.[19] compared deformation behavior between compression and tension tests of Si_3N_4 with crystalline phases of α-$Y_2Si_2O_7$ and $Y_5(SiO_4)_3N$, and have reported that the material crept nearly 100 times

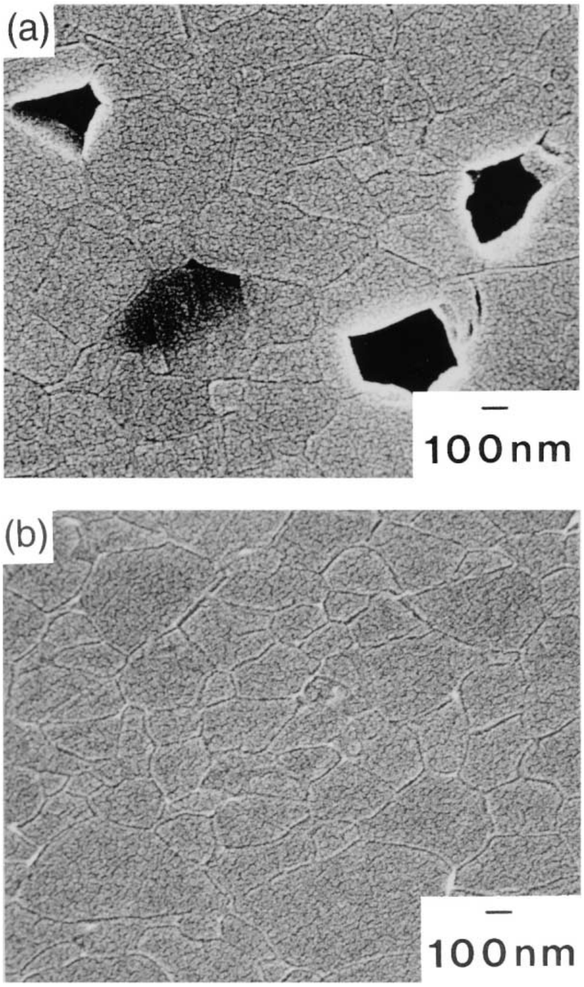

Fig. 9. SEM photographs of (a) 74% elongated SiC(G1) and (b) 153% elongated SiC(G2).

faster in tension than in compression. They suggested that cavitation in the multigrain junctions allowed the silicate to flow from cavities to surrounding silicate pockets, allowing the dilatation of the microstructure and deformation of the material in tension test.

In the case of SiC(G1) and SiC(G2), flow stresses in compression and tension tests were almost same and strain softening by cavitation damage was not observed before the true strain of 0.5 in tension test. This indicated that the contribution of cavitation for tensile deformation was a little. Therefore, the main deformation mechanisms were thought to be the same in compression and tension tests. Besides, in the case of compression tests, the argument of deformation mechanism by stress exponents can be done precisely because cavitation damage and the vaporization of grain-boundary phase are suppressed. In this experiment, stress exponents in compression tests of SiC(G1) and SiC(G2) were about 2, and extensive microstructural change was not observed. Apparently, grain-boundary phase was squeezed out by tensile deformation and collected at the triple points at elevated temperature. The contribution of the grain-boundary sliding to the total strain was calculated to be in the order of ~76% in elongated specimens of SiC(G1) and SiC(G2). Therefore, the main deformation mechanism was thought to be grain-boundary sliding in both SiC(G1) and SiC(G2).[18]

4.2. *Effect of strain rate*

Authors of this study reported the effect of strain rates for flow stresses of liquid-phase sintered β-SiC with the additions of Al_2O_3–Y_2O_3–CaO and Al_2O_3–Y_2O_3 in tension tests at elevated temperature in Ar.[7] The flow stress at high strain rate (2×10^{-4} s^{-1}) was influenced by the initial grain size and the viscosity of liquid phase. Flow stress at low strain rate (5×10^{-5} s^{-1}) was influenced by the grain growth and the vaporization of grain-boundary phase during the deformation. Therefore, this experiment at the initial strain rate of 2×10^{-5} s^{-1} was thought to be influenced by the grain growth and the vaporization of grain-boundary phase during the deformation.

4.3. *Effect of microstructural change and the viscosity of grain-boundary phase*

Grain growth during the deformation at elevated temperature causes the increase of flow stress as shown in Eq. (3). SiC(G1) after 74% elongation and SiC(G2) after 153% elongation showed 30% and 35% grain growth, respectively. Testing time of SiC(G2) was more than 2 times longer than that of SiC(G1). Therefore, the effect of grain growth for strain hardening was thought to be higher in SiC(G1).

On the other hand, the amorphous phase at grain boundaries promotes the grain-boundary sliding. Accordingly, the flow stress of material with an amorphous phase at grain boundaries is lower than that with no amorphous phase at grain boundaries. Wiederhorn et al. compared the creep rates of Si_3N_4 with different additives and have reported that the lowering of viscosity of grain-boundary phase and the increasing of total amount of grain-boundary phase enhanced the creep rate.[20] Yoshizawa and Sakuma have reported that a decrease in glass viscosity contributes to the lowering of the flow stress in yttria-stabilized tetragonal zirconia polycrystals (Y–TZP) with SiO_2 glass added.[21] In general, glass viscosity decreases with the addition of alkaline earth because alkaline earth cations disrupt the network of the Si–O bonds, causing the amount of non-bridging oxygen to increase, and the network structure weakens. The flow stress of SiC with Si–Mg–Al–Y–O glass can be noticeably lower than that of SiC with Si–Al–Y–O–N, because of the low viscosity of the grain-boundary phase, if we only consider the viscosity of the grain-boundary phase.

However, as can be seen from Table 2, SiC(G1) after 74% elongation and SiC(G2) after 153% elongation

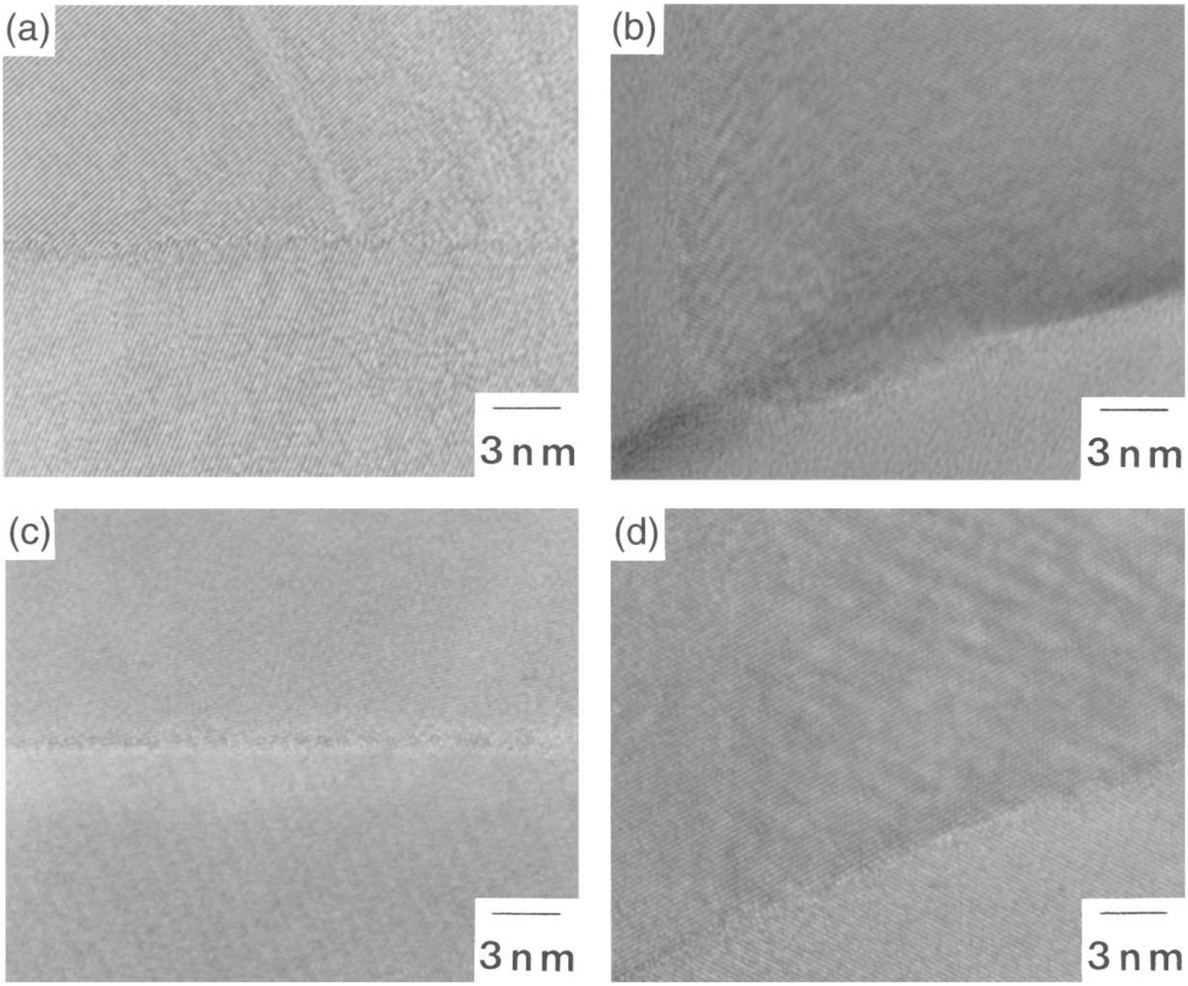

Fig. 10. HRTEM images at (a) grain boundary of SiC(G1) after 74% elongation, (b) triple point of SiC(G1) after 74% elongation, (c) grain boundary of SiC(G2) after 153% elongation and (d) triple point of SiC(G2) after 153% elongation.

showed 26.4 and 21.1 wt.% weight loss, respectively. The weight loss more than the weight of the sintering additives shows the decomposition of SiC concurrent with the vaporization of grain-boundary phase. Authors of this study have reported that the vaporization of amorphous phase at the grain boundaries contributes to the rapid increase of the flow stress during the high temperature deformation in Al-doped β-SiC.[22] Therefore, the lowering effect of flow stress by amorphous phase was thought to be short time in SiC(G1) with more volatile amorphous phase.

Cavity or void formation is a common phenomenon accompanying superplastic deformation.[23] The cavities linking and coalescing may be the origin of fracture during the superplastic deformation. In general, the cavitation damage during superplastic deformation is high in the material with low viscosity of glass phase and high flow stress. Therefore, the cavitation damage of SiC(G1) after 74% elongation was higher than that of SiC(G2) after 153% elongation as shown in Fig. 9.

Crystalline phases at triple points were observed in both fractured SiC(G1) and SiC(G2) after the tensile deformation as shown in Fig. 10. The authors of this study have reported that the formation of crystalline phase at the triple points prevented the grain-boundary sliding and was the origin of fracture during the deformation of liquid-phase sintered β-SiC.[10]

Table 2
Results of tension tests at the initial strain rate of 1×10^{-5} s^{-1} at 2023 K

Material	Time	Elongation	Weight loss	Grain size after tension test	
				$d_{\perp}$	$d_{//}$
SiC(G1)	1253 min	74%	26.4%	350 nm	500 nm
SiC(G2)	2589 min	153%	21.1%	300 nm	430 nm

5. Conclusion

Compression tests and tension tests of liquid-phase sintered β-SiC with oxynitride glasses at the constant crosshead speeds were performed by a universal testing machine in N_2 atmosphere. The results were as follows:

1. SiC(G1) and SiC(G2) showed 74 and 153% elongation at the initial strain rate of 1×10^{-5} s^{-1} at 2023 K in tension test, respectively.
2. Stress exponents in compression tests were about 2 in the temperature range from 1998 to 2023 K in both materials.
3. Strain hardening was enhanced by grain growth and vaporization of amorphous phase during deformation.
4. Most of grain-boundary phase at two-grain junctions disappeared during tension test. Most of residual grain-boundary phase existed at the triple points.
5. Crystalline phases at triple points were found in fractured tensile specimens of SiC(G1) and SiC(G2).
6. Critical deformation mechanism in both SiC(G1) and SiC(G2) was grain-boundary sliding.

Therefore, the initial grain size of the as-sintered material, the grain growth rate and the cavitation damage during deformation, the vaporization of grain-boundary phase, the formation of crystalline phases at triple points are important factors to improve the superplastic deformation behavior in liquid-phase sintered SiC with an amorphous phase.

References

1. Prochazka, S., The role of boron and carbon in the sintering of silicon carbide. In *Special Ceramics 6*, ed. P. Popper. British Ceramic Research Association, Stoke-on-Trent, 1975, pp. 171–181.
2. Suzuki, H., Recent trend and theoretical background in sintering process of silicon carbide. *Ceramics,* 1983, **18**(1), 3–9.
3. Shinoda, Y., Nagano, T., Gu, H. and Wakai, F., Superplasticity of silicon carbide. *J. Am. Ceram. Soc.,* 1999, **82**(10), 2916–2918.
4. Gu, H., Shinoda, Y. and Wakai, F., Detection of boron segregation to grain boundaries in silicon carbide by spatially resolved electron energy-loss spectroscopy. *J. Am. Ceram. Soc.,* 1999, **82**(2), 469–472.
5. Nagano, T., Honda, S., Wakai, F. and Mitomo, M., Compressive deformation of liquid-phase sintered silicon carbide at elevated temperature. In *Superplasticity & Superplastic Forming 1998*, ed. A. K. Ghosh and T. R. Bieler. The Minerals, Metals & Materials Society, Warrendale, 1998, pp. 247–256.
6. Nagano, T., Honda, S., Wakai, F. and Mitomo, M., Deformation of liquid-phase sintered silicon carbide at elevated temperature. In *Ceramic Materials Components for Engines*, ed. K. Niihara, S. Hirano, S. Kanzaki, K. Komeya and K. Morinaga. Japan Fine Ceramics Association, Tokyo, 1997, pp. 707–712.
7. Nagano, T., Gu, H., Shinoda, Y., Zhan, G.-D., Mitomo, M. and Wakai, F., Tensile ductility of liquid-phase sintered β-silicon carbide at elevated temperature. *Mater. Sci. Forum,* 1999, **304/306**, 507–512.
8. Nagano, T., Gu, H., Shinoda, Y., Mitomo, M. and Wakai, F., Tensile ductility of liquid-phase sintered β-silicon carbide at elevated temperature. In *Ceramics: Getting into The 2000's, Part D*, ed. P. Vincenzini. Techna, Faenza, 1999, pp. 25–32.
9. Nagano, T., Kaneko, K., Zhan, G.-D. and Mitomo, M., Effect of atmosphere on weight loss in sintered silicon carbide during heat treatment. *J. Am. Ceram. Soc.,* 2000, **83**(11), 2781–2787.
10. Nagano, T., Gu, H., Kaneko, K., Zhan, G.-D. and Mitomo, M., Effect of dynamic microstructural change on deformation behavior in liquid-phase-sintered silicon carbide with Al_2O_3–Y_2O_3–CaO additions. *J. Am. Ceram. Soc.*, in press.
11. Nagano, T., unpublished work.
12. Jun, H.-W., Lee, H.-W., Kim, G.-H., Song, H. and Kim, B.-H., Effect of sintering atmosphere on the microstructure evolution and mechanical properties of silicon carbide ceramics. *Ceram. Eng. Sci. Proc.,* 1997, **18**(4), 487–504.
13. Kim, Y.-W. and Mitomo, M., Fine-grained silicon carbide ceramics with oxynitride glass. *J. Am. Ceram. Soc.,* 1999, **82**(10), 2731–2736.
14. Elmer, T. H. and Nordberg, M. E., Effect of nitriding on electrolysis and devitrification of high-silica glasses. *J. Am. Ceram. Soc.,* 1967, **50**(6), 275–279.
15. Mukherjee, A., Bird, J. E. and Dorn, J. E., Experimental correlations for high temperature creep. *Trans. ASM,* 1969, **62**(1), 155–179.
16. Tanaka, H. and Iyi, N., Simple calculation of SiC polytype contents from powder X-ray diffraction peaks. *J. Ceram. Soc. Jpn.,* 1993, **101**(11), 1313–1314.
17. Kashyap, B. P., Ariel, A. and Mukherjee, A. K., Review: microstructural aspects of superplasticity. *J. Mater. Sci.,* 1985, **20**(8), 2661–2686.
18. Nagano, T., Kaneko, K., Zhan, G. D. and Mitomo, M., Superplasticity of liquidphase-sintered β-SiC with Al_2O_3–Y_2O_3–AlN additions in an N_2 atmosphere. *J. Am. Ceram. Soc.,* 2000, **83**(10), 2497–2502.
19. Luecke, W. E., Wiederhorn, S. M., Hockey, B. J., Krause, R. F., Jr. and Long, G. G., Cavitation contributes substantially to tensile creep in silicon nitride. *J. Am. Ceram. Soc.,* 1995, **78**(8), 2085–2096.
20. Wiederhorn, S. M., High temperature deformation of silicon nitride. *Z. Metallkd.,* 1999, **90**(12), 1053–1058.
21. Yoshizawa, Y. and Sakuma, T., Role of grain-boundary glass phase on the superplastic deformation of tetragonal zirconia polycrystal. *J. Am. Ceram. Soc.,* 1990, **73**(10), 3069–3073.
22. Nagano, T., Kaneko, K. and Kodama, H., Tensile ductility of Al-doped β-silicon carbide at elevated temperature. In *The Third Pacific Rim International Conference on Advanced Materials and Processing (PRICM3)*, ed. M. A. Imam, R. DeNale, S. Hanada, Z. Zhong and D. N. Lee. The Minerals, Metals & Materials Society, Warrendale, 1998, pp. 1897–1902.
23. Stowell, M.J., Cavitation in superplasticity. In *Superplastic Forming of Structural Alloys*, ed. N. E. Paton and C. H. Hamilton. Metallurgical Soc. of AIME, 1982, pp. 321-326.